JGR Space Physics

RESEARCH ARTICLE
10.1029/2020JA028625

Key Points:
- The eclipse obscuration would lead to a TEC reduction of up to ~4.5 TECu (~22%)
- Electron and oxygen ion temperatures are expected to decrease up to ~400 (~22%) and ~200 K (~8%), respectively
- Magnetically conjugate reductions of up to ~1.5 TECu (~5%) are predicted

Supporting Information:
- Supporting Information S1

Correspondence to:
M. Martínez-Ledesma,
mimartinezl@udec.cl

Citation:
Martínez-Ledesma, M., Bravo, M., Urra, B., Souza, J., & Foppiano, A. (2020). Prediction of the ionospheric response to the 14 December 2020 total solar eclipse using SUPIM-INPE. *Journal of Geophysical Research: Space Physics*, *125*, e2020JA028625. https://doi.org/10.1029/2020JA028625

Received 24 AUG 2020
Accepted 22 OCT 2020
Accepted article online 3 NOV 2020

Prediction of the Ionospheric Response to the 14 December 2020 Total Solar Eclipse Using SUPIM-INPE

M. Martínez-Ledesma[1,2], M. Bravo[3,4], B. Urra[3], J. Souza[5], and A. Foppiano[3,4]

[1]CePIA, Departamento de Astronomía, Universidad de Concepción, Concepción, Chile, [2]Departamento de Física, Universidad de Santiago de Chile, Santiago, Chile, [3]Departamento de Geofísica, Universidad de Concepción, Concepción, Chile, [4]Centro Interuniversitario de Física de la Alta Atmósfera, Concepción, Chile, [5]Instituto Nacional de Pesquisas Espaciais, INPE, São José dos Campos, Brazil

Abstract We present the first prediction of the ionospheric response to the 14 December 2020 solar eclipse using the SUPIM-INPE model. Simulations are made for all known ionosonde stations for which solar obscuration is significant. The found response is similar to that previously reported for other eclipses, but it also shows a modification of the equatorial fountain transport that will impact the low latitudes after the event. In addition to the large reduction of electron concentration along the totality path (~4.5 TECu, ~22%), a significant electron and oxygen ion temperature cooling is observed (up to ~400 K) followed by lasting temperature increases. Changes of up to ~1.5 TECu (~5%) are also expected at the conjugate hemisphere. These predictions may serve as a reference for eventual ionospheric measurements of multiple instruments and are leading to a better understanding of the ionospheric response to solar eclipses.

1. Introduction

On 14 December 2020, a total solar eclipse (TSE) will be observed in South America, being the second eclipse occurring at this region in just over a year, a so-called "South American Eclipse Season" period. The eclipse totality path will start on the continent at 16.02 UT (11.18 SAT), 69 km southwest of Temuco (38.7°S, 72.6°W), Chile, and end at 16.40 UT (11.87 SAT), 250 km south of Bahia Blanca (38.9°S, 62.2°W), Argentina. During the eclipse, the Moon will partially block the solar extreme ultraviolet (EUV) irradiation of the Earth's atmosphere, disturbing the production and dynamics of the ionosphere. The predictability of the sudden decrease and posterior increase of the solar radiation provides an excellent opportunity to experimentally study the ionosphere (Beynon, 1955; Jose et al., 2020; Rishbeth, 1968).

Using several experimental approaches, it has been demonstrated that different ionospheric effects arise during the solar obscuration (e.g., see Adekoya & Chukwuma, 2016; Afraimovich et al., 2002; Evans, 1965a; Le et al., 2008a; Ratcliffe, 1956; Rishbeth, 1968). Generally, in the lower ionosphere (E and F_1 layers), well-known recombination processes lead to a large depletion of electron concentration due to the lack of photoionization, while at the higher altitudes, more complex processes interplay to explain the large variability observed. In particular, the ionospheric response to an eclipse depends on the solar and geomagnetic activity, local time, lower atmospheric interactions, plasma diffusion and transport processes, and the specific geometry of the eclipse, that is, different totality paths at the different ionospheric heights and times (Verhulst & Stankov, 2020). Moreover, the response has been shown to be strongly dependent on latitude (Le, Liu, Yue, & Wan, 2009). At the magnetic equator and low geomagnetic latitudes, the plasma electrodynamic processes dominate the response to the eclipse, particularly the fountain effect and the Equatorial Ionization Anomaly (EIA; Adekoya & Chukwuma, 2016; Bravo et al., 2020; Cheng et al., 1992; Jonah et al., 2020; Jose et al., 2020; Le, Liu, Yue, & Wan, 2009; Madhav Haridas & Manju, 2012; Sridharan et al., 2002; Tomás et al., 2007; Tsai & Liu, 1999).

Many different ionospheric models have been used to determine the effects of eclipses, such as the NCAR model (Roble et al., 1986; Salah et al., 1986), CTIP (Müller-Wodarg et al., 1998), SUPIM (Bravo et al., 2020; MacPherson et al., 2000), TIME-IGGCAS (Le et al., 2008a, 2008b; Le, Liu, Yue, & Wan, 2009; Le, Liu, Yue, Wan, & Ning, 2009; Le et al., 2010), SAMI3 (Huba & Drob, 2017), FLIP (Reinisch et al., 2018; Unnikrishnan & Richards, 2014), GITM (Cnossen et al., 2019; Wu et al., 2018), TIEGCM

(Chen et al., 2019; Dang et al., 2018, 2020; Lei et al., 2018; Wang et al., 2019), WACCM-X (McInerney et al., 2018), and an empirical ionospheric model based on measurements of the Millstone Hill incoherent scatter radar (ISR; Goncharenko et al., 2018). However, few studies estimate the ionospheric impacts prior to eclipses occurrence (Dang et al., 2020; Huba & Drob, 2017; Müller-Wodarg et al., 1998). Such predictions provide a reference to eventual observations, helping to improve the quality of the measurements.

The 14 December 2020 eclipse is an opportunity to confirm and improve the knowledge on the response of the low-latitude ionosphere already gained from the analysis of the 2 July 2019 eclipse (Bravo et al., 2020). Indeed, the low-latitude response to eclipses is a process yet not fully understood (Dang et al., 2020). Here we provide the first prediction of the ionospheric response to the solar eclipse of 14 December 2020 using the Sheffield University Plasmasphere Ionosphere Model (Bailey & Sellek, 1990; Bailey et al., 1993) adapted at the Instituto Nacional de Pesquisas Espaciais (SUPIM-INPE). Simulations also include midlatitude locations so as to help interpreting eventual observations for these latitudes.

2. Model

The SUPIM-INPE model accurately reproduces the low-latitudinal ionospheric effects over South America (Bravo et al., 2017, 2019; Nogueira et al., 2013; Santos et al., 2016; Souza et al., 2010, 2013). Moreover, the SUPIM model has been used to qualitatively reproduce observations at midlatitudes (Balan et al., 1995; Thampi et al., 2011). This model solves the time-dependent equations of continuity, momentum, and energy balance along closed magnetic field lines for the most relevant ion species (O^+, H^+, He^+, N_2^+, NO^+, N^+, and O_2^+). The INPE version implements the E region chemical reaction scheme applied by Huba et al. (2000), the NRLMSISE-00 model (Picone et al., 2002) for neutral densities, the HWM93 model (Hedin et al., 1996) for neutral winds, and the $E \times B$ vertical drift of the model of Fejer et al. (2008). The photoionization of neutral gases is calculated using the model of EUV irradiance developed by Richards et al. (2010) based on measurements of the Solar EUV Experiment (SEE) instrument on the TIMED satellite (Woods et al., 2005, 2008). Nevertheless, at wavelengths smaller than 27 nm the HEUVAC model (Richards et al., 2006) is used since TIMED/SEE measured fluxes underestimate solar irradiances at this wavelength range (Peterson et al., 2009; Strickland et al., 2007; Woods et al., 2008). Solar flux and geomagnetic activity indices considered in simulation are $Ap = 5.9$ and $F_{10.7}/F_{10.7A} = 76.5$ s.f.u., as predicted using the 13 month smoothed long-range estimation method of Niehuss et al. (1996). The model is run in 5 min steps and with a magnetic latitude resolution of 0.25°.

To simulate the irradiation reduction during the eclipse, the input radiation is modified by an eclipse obscuration mask (***ObscMask***), shown in Figure 1. To determine the percentage of solar radiation reduction, the geometry of the solar occultation is calculated at different times and locations using the library of Frissell (2017). ***ObscMask*** values are calculated with a latitudinal and longitudinal resolution of 0.25°. This mask is for a 300 km altitude, which corresponds to the approximate altitude of the maximum ionospheric concentration. Note that there are small mask geometric differences for altitudes between 100, 350, and 500 km (as it can be seen in Figure 6 of Verhulst & Stankov, 2020). Moreover, the larger differences for altitudes higher than 500 km generate only a small ionospheric impact since the electron concentrations are much smaller. Thus, it is considered that the ionospheric response to the eclipse can be accurately represented by using the obscuration mask at 300 km altitude.

During the eclipse totality, the solar chromosphere is completely blocked by the Moon, but part of the coronal radiation still contributes to the ionospheric photoionization. The coronal radiation (wavelengths below 30 nm) generates photoelectrons corresponding to only 2% of the total photoionization rate and are mainly responsible for the ionization below 200 km (Reinisch et al., 2018). There are different approaches to determine the amount of coronal soft-X-ray and EUV emission that remains during totality. Cnossen et al. (2019) considered a 10% of coronal contribution, Huba and Drob (2017) and Mrak et al. (2018) a 15%, Le et al. (2008b) and Dang et al. (2018) a 22%, and Reinisch et al. (2018) and Bravo et al. (2020) used a 30%. The 30% is the value that provided the best fit to the electron concentration variation at 150 km in Reinisch et al. (2018), which used the TIMED/SEE (Richards et al., 2010) irradiance model. Note that the total solar XUV/EUV irradiance varies with the number of solar active regions (Huba & Drob, 2017) and that the EUV obscuration mask is dependent on the solar flares active during the eclipse (Mrak et al., 2018). In our work the SUPIM-INPE model was run with 15% and 30% coronal emission contributions to determine

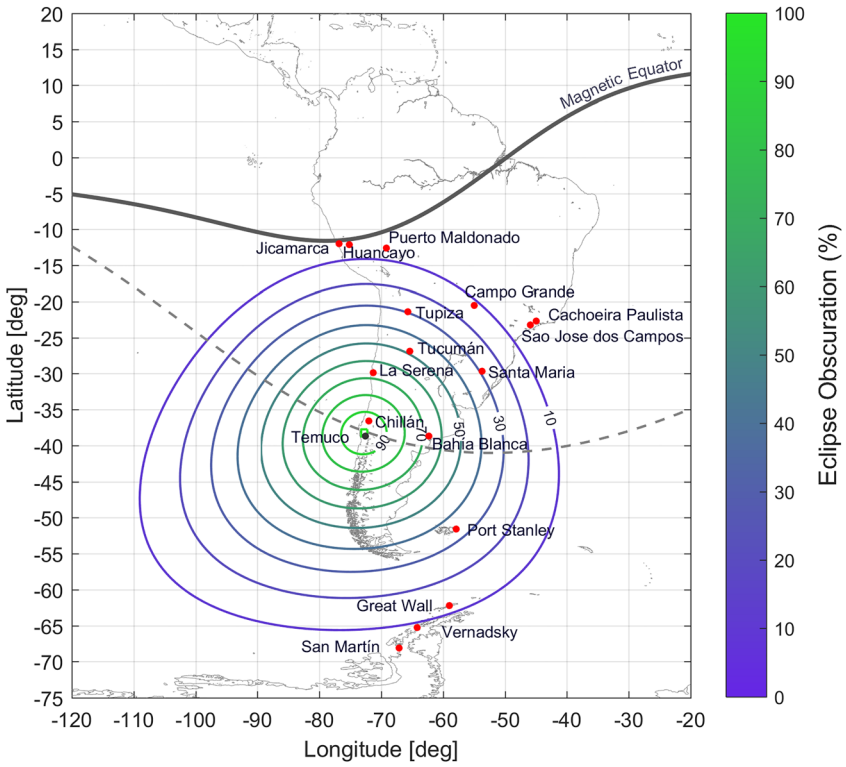

Figure 1. Eclipse obscuration mask at 300 km height during the maximum obscuration time (16.03 UT) over Temuco (black dot). South American and Antarctic ionosonde stations (red dots) with solar radiation reduction >8% (see Table 1). Totality path at 300 km (dashed gray line) calculated as per Verhulst and Stankov (2020).

the differences of control and eclipse simulations. It was found that differences are smaller than ~2% for TEC, E, and F_2 layers critical frequencies. The maximum difference for the F_1 layer critical frequency is ~8%, confirming that the EUV coronal reduction mainly impacts at these altitudes, as suggested by Reinisch et al. (2018). Here, it is assumed that 30% of the coronal emissions remain during totality. Future work is required to determine the exact coronal contribution and EUV obscuration mask by measuring the emissions coming from the solar disk during the eclipse, following the procedure indicated by Mrak et al. (2018).

Therefore, for a given wavelength ($\boldsymbol{\lambda}$), the modified solar input radiation ($\boldsymbol{I_R}$) is expressed as

$$\boldsymbol{I_R = I_{NT} + I_{R0}^{\lambda < 30.4}\,(1 - 0.7 \times ObscMask) + I_{R0}^{\lambda \geq 30.4}\,(1 - ObscMask)}, \quad (1)$$

where $\boldsymbol{I_{NT}}$ is the nighttime radiation calculated as per Strobel et al. (1974; Souza et al., 2010), $\boldsymbol{I_{R0}^{\lambda < 30.4}}$ and $\boldsymbol{I_{R0}^{\lambda \geq 30.4}}$ are the ionizing radiations for $\lambda < 30.4$ nm (coronal range) and $\lambda \geq 30.4$ nm (chromospherical range), respectively, and ***ObscMask*** is the normalized value of the obscuration mask (i.e., 0 and 1 correspond to no-eclipse and eclipse totality cases, respectively).

3. Results and Discussion

The ionosonde stations for which the solar obscuration during the eclipse is larger than 8% are shown in Figure 1. The corresponding eclipse times and maximum percentage of solar radiation reduction at 300 km height are listed in Table 1. These parameters were also calculated at Temuco (TE; 38.7°S, 72.6°W), Chile, the only large population city at the totality path of the eclipse at 300 km height. Simulation results for these stations are provided in the supporting information to help compare with forthcoming measurements.

Figure 2 shows the control and eclipse-modified simulation values of total electron content (TEC), critical frequencies (f_oE, f_oF_1, and f_oF_2), and peak heights (h_mE and h_mF_2) of the different ionospheric layers at four selected stations: within the totality path, Temuco (TE: 38.7°S, 72.6°W), and at three locations that provide

10.1029/2020JA028625

Table 1
Ionosonde Stations Impacted by the Eclipse

Station name	Geographic latitude (degrees)	Geographic longitude (degrees)	Magnetic latitude (degrees)	Eclipse start time (EST) (UT)	Eclipse maximum obscuration time (MOT) (UT)	Eclipse end time (EET) (UT)	Maximum percentage of obscuration (MPO) (%)	ΔTEC		Δf_oF_2		Δf190		Δf_oE	
								TECu	%	MHz	%	MHz	%	MHz	%
Jicamarca (JI)	−12.0	283.2	−1.5	14.20	15.21	16.34	17	1.5	7	0.4	6	0.2	6	0.2	4
Huancayo (HU)	−12.1	284.8	−1.8	14.29	15.28	16.41	15	1.3	6	0.4	6	0.2	5	0.1	4
Puerto Maldonado (PM)	−12.6	290.8	−3.3	14.68	15.61	16.63	8	0.8	4	0.2	3	0.1	3	0.1	2
Campo Grande (CG)	−20.5	305.0	−15.3	15.42	16.70	17.92	20	1.7	6	0.3	3	0.3	7	0.2	5
Tupiza (TZ)	−21.4	294.3	−12.8	14.70	16.03	17.45	30	2.4	9	0.4	4	0.4	10	0.3	8
Cachoeira Paulista (CP)	−22.7	315.0	−21.0	15.93	17.25	18.42	30	2.0	7	0.4	4	0.4	10	0.3	8
Sao Jose dos Campos (SJ)	−23.2	314.1	−21.0	15.86	17.21	18.40	31	2.1	8	0.5	5	0.4	10	0.3	8
Tucuman (TU)	−26.9	294.6	−18.0	14.70	16.15	17.68	49	3.4	14	0.7	8	0.8	18	0.5	15
Santa Maria (SA)	−29.7	306.3	−23.8	15.28	16.79	18.21	54	3.4	13	0.7	7	0.8	19	0.6	16
La Serena (LS)	−29.9	288.7	−19.8	14.48	15.93	17.48	68	4.2	17	0.9	10	1.1	26	0.8	22
Chillan (CH)	−36.6	288.0	−26.3	14.61	16.03	17.55	95	4.6	18	1.0	11	1.8	43	1.5	42
Temuco (TE)	−38.7	287.4	−28.3	14.63	16.03	17.54	100	4.5	17	1.0	11	2.0	46	1.7	46
Bahia Blanca (BB)	−38.7	297.7	−30.0	14.95	16.44	17.93	95	4.4	17	0.9	10	1.8	42	1.5	42
Port Stanley (PS)	−51.6	302.1	−43.3	15.37	16.63	17.85	60	2.0	11	0.5	7	0.9	22	0.7	19
Great Wall (GW)	−62.2	301.0	−53.0	15.65	16.58	17.51	26	0.8	5	0.3	5	0.4	8	0.2	7
Vernadsky (VE)	−65.3	295.8	−55.5	15.69	16.50	17.31	17	0.5	3	0.2	3	0.2	5	0.2	4
San Martin (SM)	−68.1	292.9	−58.0	15.78	16.47	17.15	11	0.3	2	0.1	1	0.1	3	0.1	3

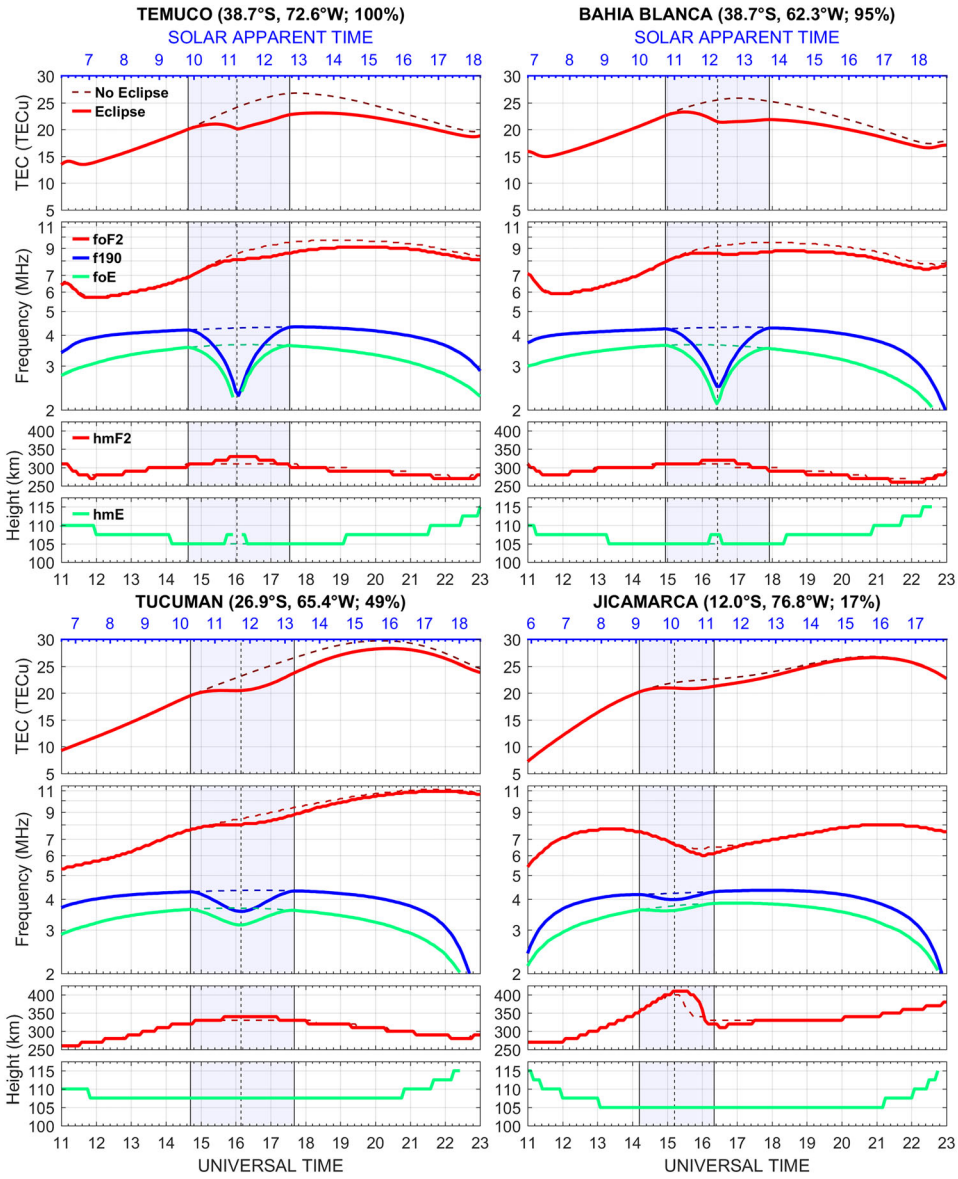

Figure 2. Control (dashed lines) and eclipse (continuous lines) simulation values of TEC, f_oF_2, $f190$, f_oE, h_mF_2, and $h_mE$at different stations. Only E layer frequencies higher than 2 MHz are determined. Eclipse times (vertical lines) and maximum percentages of obscuration are calculated at 300 km height in each station.

the best latitudinal and longitudinal distribution of eclipse effects, that is, Bahia Blanca (BB; 38.7°S, 62.3°W), Tucuman (TU; 26.9°S, 65.4°W), and Jicamarca (JI; 12.0°S, 76.8°W), with maximum obscurations of 95%, 49%, and 17%, respectively. Note that f_oF_1 is taken as the plasma frequency from the simulated $N(h)$ distributions at 190 km ($f190$). This procedure minimizes the f_oF_1 uncertainty due to the large variability of F_1 layer $N(h)$ and its inherent identification difficulty (e.g., Li et al., 2019) and is consistent with a well-defined f_oF_1 diurnal variation (Reinisch & Huang, 1996).

In all four stations (Figure 2), f_oE and $f190$ show a reduction following the decrease of solar radiation and achieve their minimum values during the maximum obscuration time (MOT). After the MOT, f_oE and $f190$ gradually recover and reach the values of control simulations at the eclipse end time (EET), similarly as found in previous studies (Adekoya et al., 2015; Cheng et al., 1992). Near the totality path (TE), during the MOT, foE tends to zero (E layer density depletion), but $f190$ does not due to the way it is determined. Alternatively, at BB, with a maximum obscuration of 95%, foE does not tend to 0 (complete E layer depletion), although this effect may be related to the temporal resolution of the model. TU and JI, with lesser obscuration

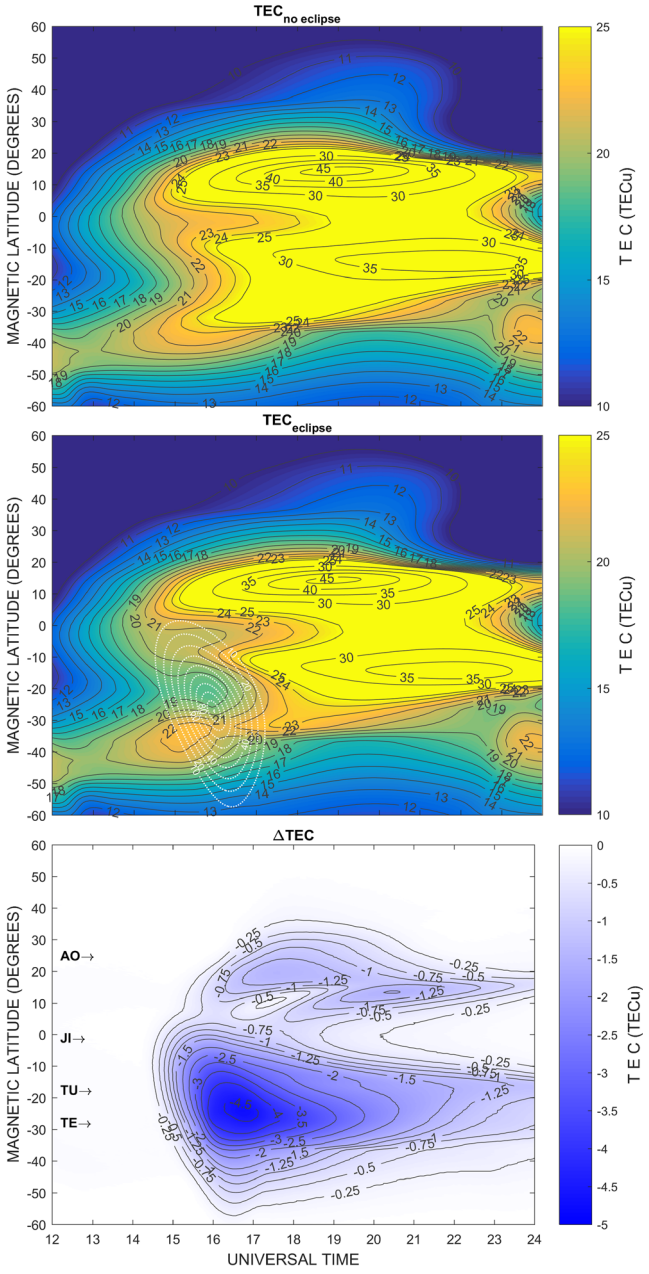

Figure 3. TEC time evolution for control (top) and eclipse-modified (middle) simulations, and their difference (bottom) along the magnetic meridian of Jicamarca. Evolution of the eclipse obscuration mask at 300 km height (white dotted lines). Magnetic latitudes of Temuco (TE; 38.7°S, 72.6°W), Tucuman (TU; 26.9°S, 65.4°W), Jicamarca (JI; 12.0°S, 76.8°W), and Arecibo Observatory (AO; 18.3°N, 66.8°W) are represented with horizontal arrows.

levels, show much smaller reductions of both f_oE and f190. Moreover, little h_mE changes are observed during the eclipse.

By contrast, TEC and f_oF_2 exhibit a delayed response, as found in previous studies (e.g., Adekoya et al., 2015; Bravo et al., 2020). At all these stations (TE, BB, TU, and JI) these parameters do not decrease during the initial part of the eclipse, showing the maximum reduction after the MOT. The recovery is slow, reaching the control simulation values after at least ~5 hr. TU, located near the ionospheric southern EIA crest (Pezzopane et al., 2007), shows the largest f_oF_2 and TEC values, with maxima at ~21 UT. At the first three stations, very small increases of h_mF_2 are found during the eclipse. At the magnetic equator (JI), the maximum reduction of f_oF_2 and TEC is attained at the EET, ~1 hr after MOT, also showing very small recovery times to reach control values. Moreover, h_mF_2 largely increases reaching a peak after the MOT, followed by a sharp drop below control values. This behavior coincides with the noon uplift related to the daytime upward $E \times B$ drift (Lee et al., 2008). Very similar results for equatorial f_oF_2 and h_mF_2 variations were reported by Adeniyi et al. (2007). This intense uplift suggests that the equatorial response is largely dominated by the fountain effect (Adekoya et al., 2015; Cheng et al., 1992; Le, Liu, Yue, & Wan, 2009). It is worth noting that these eclipse responses compete with vertical drift and other transport processes (Adekoya et al., 2015) and that very different responses could be found depending on the variability of equatorial processes (e.g., Bravo et al., 2020; Jonah et al., 2020).

The maximum reduction values of TEC, f_oF_2, f190, and f_oE predicted for each station are indicated in Table 1. These decreases shows a linear dependence on the maximum percentage of obscuration (MPO) at 300 km height (slopes of ~0.044 TECu/MPO for TEC, ~0.009 MHz/MPO for f_oF_2, ~0.020 MHz/MPO for f190, and ~0.017 MHz/MPO for f_oE, as shown in supporting information Figure S1). The F_1 and E layers display the largest reduction, reaching frequency reductions of up to ~46% at TE in both layers. Alternatively, the F_2 layer presents a smaller decrease (only 11% within the totality path) and a more variable dependency on solar radiation reduction. These effects agree with previous studies that indicate the depletion of E and F_1 layers due to recombination processes and large variability in the F_2 layer (e.g., Rishbeth, 1968). Furthermore, midlatitudes stations, such as Port Stanley (PS; 51.6°S, 57.9°W), Great Wall (GW; 62.2°S, 59.0°W), Vernadsky (VE; 65.3°S, 64.2°W), and San Martin (SM; 68.1°S, 67.1°W), exhibit smaller f_oF_2 and TEC reductions than other stations with similar MPO values, confirming the large latitudinal dependence of eclipse impacts (Le, Liu, Yue, & Wan, 2009). These results also suggest impacts at the Weddell Sea Anomaly (Li et al., 2018).

Figure 3 shows the temporal evolution of TEC for the control (top) and eclipse-modified (middle) simulations along the magnetic meridian of JI. The difference between these simulations (Figure 3, bottom) shows a maximum dip of ~4.5 TECu (~22%) above the magnetic latitude of TE after its MOT (16.03 UT). Furthermore, at magnetic latitudes near the southern EIA crest, near TU, the eclipse impact displays the longest duration, with a reduction >1 TECu for more than 7 hr after the event. This result confirms that the equatorial and low-latitude eclipse impacts are regulated by the fountain effect (Cheng et al., 1992; Le, Liu, Yue, & Wan, 2009) and vice versa.

Two dips are observed in Figure 3 (bottom) at the northern magnetic hemisphere. The first TEC reduction shows a maximum decrease of ~1.25 TECu at locations near the magnetic conjugate of the totality path (TE), starting approximately at the MOT. This conjugate effect could be measured at the Arecibo

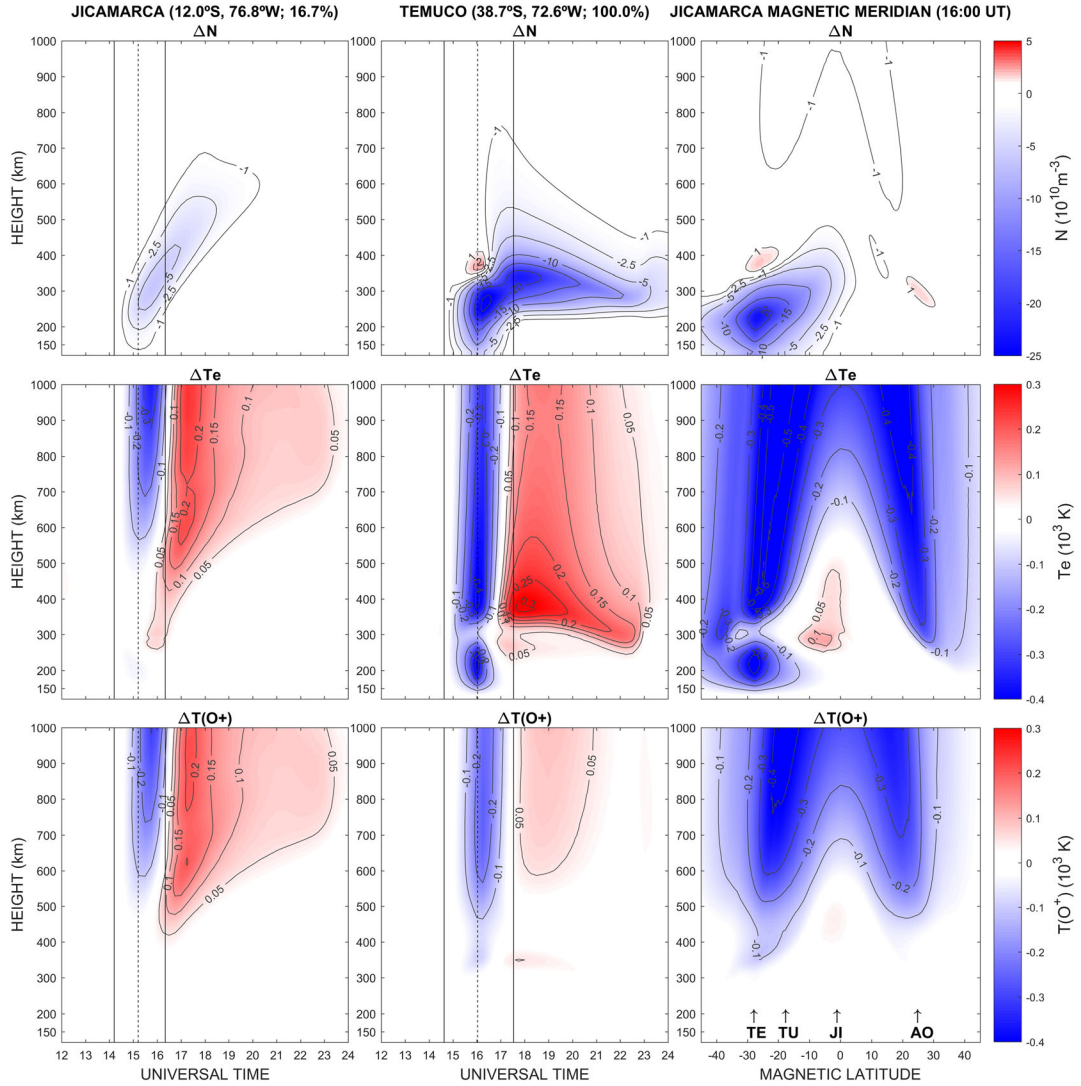

Figure 4. Vertical distribution of the control and eclipse-modified differences of electron concentration (ΔN), and electron (ΔT_e) and oxygen ion (ΔT_O+) temperatures over time in Jicamarca (left column) and Temuco (middle column), and along the magnetic meridian of Jicamarca at 16:00 UT (right column). Magnetic latitudes of the stations indicated in Figure 3 (TE, TU, JI, and AO) are represented with vertical arrows.

Observatory (AO; 18.3°N, 66.8°W) or Ramey (18.5°N, 67.1°W). This reduction can be related to a large northward interhemispheric plasma flux as deduced from the large asymmetry displayed in TEC (see top and middle panels). Similar conjugate effects have been reported for previous eclipses (e.g., Chen et al., 2019; He et al., 2018; Le, Liu, Yue, Wan, & Ning, 2009). The second reduction event shows a maximum decrease up to ~1.5 TECu at the northern EIA crest which starts after the EET (~18 UT). This second minimum may be associated to the equatorial fountain effect time evolution that becomes dominant due to the weakness of the interhemispheric flux deduced by the tendency of TEC symmetry.

Figure 4 shows the height-time distribution of control and eclipse-modified simulations differences of electron concentration ($\boldsymbol{N}$) and electron and oxygen ion temperatures ($\boldsymbol{T_e}$ and $\boldsymbol{T_{O+}}$) at the magnetic equator (JI) and within the path of totality (TE). At JI, the concentration differences show a decrease that starts at ~200 km during the initial phase of solar reduction, reaches an ~13% maximum decrease at ~250 km during the MOT, and increases in altitude over time, reaching an ~750 km maximum altitude at ~18 UT. The maximum altitude uplift time at the magnetic equator coincides with the start of the second TEC dip at the northern EIA crest found several hours after the EET (Figure 3). Therefore, this uplift is consistent with the previous assumption that the second northern TEC dip event is generated by an equatorial fountain

transport modification. Equatorial T_e and T_{O+} suffer a decrease of ~300 K (~10%) at the topside ionosphere (at altitudes >900 km with its maximum ~30 min after the MOT) and a latter increase of ~200 K (~15%) that starts at lower altitudes (>550 km with its maximum ~1 hr after the EET).

A much larger reduction of electron concentration is displayed along the totality path. At TE, a maximum depletion of ~65% is reached below ~250 km during the MOT, confirming the disappearance of E and F_1 layers. Additionally, an increase of concentration of ~2% is found at ~350 km during the totality. This increase is related to an uplift of the F_2 layer above its maximum height (and therefore not reflected in h_mF_2) associated with common nocturnal F_2 layer uplift processes (e.g., Schunk & Nagy, 2009).

Moreover, at TE, during the totality, a T_e cooling is displayed at different altitude ranges: between 150 and 250 km and at altitudes >300 km, with a maximum decrease of ~400 K (~22%) at 400 km during the MOT. Similarly as in JI, these temperature reductions are followed by a small rise which begins after the MOT, and ends ~6 hr after the EET. At TE, this rise presents a maximum increase of ~300 K (~22%) at ~350 km. Furthermore, T_{O+} values within the totality path show a similar pattern at altitudes >400 km, with maximum decrease and increase values of ~200 (~8%) and ~50 K (~3%), respectively. Similar T_e decreases and later increases during eclipses were previously modeled (e.g., Roble et al., 1986) and measured using ISR (Evans, 1965b; MacPherson et al., 2000; Sterling et al., 1972). Furthermore, a similar decrease and later increase of ion temperatures were measured by Goncharenko et al. (2018).

Previous in situ measurements at high altitudes have shown that model electron temperature differ from observations albeit following the height distribution overall shape (Hairston et al., 2018). Moreover, topside eclipse measurements of ion composition, velocity, and temperature (Yau et al., 2018) and TEC using the radio occultation technique (Perry et al., 2019) are also not well reproduced by various ionospheric models. Future work will be required to evaluate the model performance by comparing our results to satellite observations.

Figure 4 also displays the high-latitude distribution of the differences in electron concentration and temperatures along the magnetic meridian of JI around the time of totality at TE (16 UT). As expected, the maximum concentration reduction is found near the magnetic latitude of TE below 250 km, together with a small increase of concentration at ~400 km. Additionally, a concentration increase of ~2% is found at 300 km height in the vicinity of the conjugate of TE (near AO). Because of the small amplitude of this enhancement, the feature is not shown in Figure 3. Much larger concentration increases were found at conjugate locations by Le, Liu, Yue, Wan, and Ning (2009). Nevertheless, the TEC interhemisphere ratio during the control day calculated by Le, Liu, Yue, Wan, and Ning (2009) is much larger than in our simulations. This suggests that in our case the conjugate eclipse impact is much smaller. On the other hand, our results show a much large concentration decrease at conjugate locations after the eclipse maximum obscuration, as shown in the TEC (Figure 3). Small-amplitude TEC increases prior to much larger depletions were previously found at conjugates (He et al., 2018; Huba & Drob, 2017; Sergeenko, 2018). Results also show a T_e cooling along the magnetic meridian up to the Northern Hemisphere, in agreement with Huba and Drob (2017). Similar interhemispheric distribution effects are also present in the cooling of T_{O+}. These conjugate temperature decreases are originated by the photoelectron heating reduction induced by the solar obscuration. Above 300 km, the large thermal conductivity of photoelectrons along magnetic field lines allows their transfer between hemispheres, reducing the temperatures along these lines (Huba & Drob, 2017; Le, Liu, Yue, Wan, & Ning, 2009; Sergeenko, 2018).

4. Summary

The response to the upcoming 14 December 2020 eclipse has been modeled for several ionosonde stations in South America using SUPIM-INPE. A TEC decrease of up to ~4.5 TECu (~22%) is expected along the totality path, together with a maximum electron concentration depletion of ~65% below 250 km. Electron and oxygen ion temperatures are expected to decrease during totality to up to ~400 (~22%) and ~200 K (~8%), respectively. A later increase of electron temperature below ~300 K (~22%) is also simulated. Away from the totality path, the decrease of TEC shows a linear dependence on the obscuration percentage (with a slope of ~0.044 TECu/MPO). At the magnetic equator, only a small decrease in electron concentration <13% is expected during the eclipse. Nevertheless, this concentration reduction near the magnetic equator

disturbs the fountain transport, generating a low-latitudinal response several hours after the eclipse event, with a reduction up to ~1.5 TECu (~5%) at the EIA crests. Moreover, electron and oxygen ion temperatures are expected to decrease ~300 (~10%) and ~200 K (~10%), respectively, with later increases of ~200 K (~15%). Additionally, temperatures reductions are found along the magnetic field lines up to conjugate locations, as reported in previous studies. Northern Hemisphere conjugate variations of up to ~1.25 TECu are also predicted.

Acknowledgments
HEUVAC and SEE models were kindly provided by P. Richards. Solar flux and geomagnetic activity index values were obtained from NASA Marshall Solar Cycle Forecast (https://www.nasa.gov/msfcsolar/) updated on 10 July 2020. The authors wish to thank the reviewers for their assistance in evaluating this paper. M. Martínez-Ledesma acknowledges the support of Comité Mixto ESO-Chile ORP061/19 and AFOSR Project Number FA9550-19-1-0384. M. Bravo acknowledges CONICYT/FONDECYT POSTDOCTORADO 3180742. J. R. Souza would like to thank CNPq (307181/2018-9) and INCT GNSS-NavAer supported by CNPq (465648/2014-2), FAPESP (2017/50115-0), and Coordenação de Aperfeiçoamento de Pessoal de Nível Superior (CAPES) (88887.137186/2017-00).

References

Adekoya, B. J., & Chukwuma, V. U. (2016). Ionospheric F_2 layer responses to total solar eclipses at low and mid-latitude. *Journal of Atmospheric and Solar-Terrestrial Physics*, *138–139*, 136–160, ISSN 1364-6826. https://doi.org/10.1016/j.jastp.2016.01.006

Adekoya, B. J., Chukwuma, V. U., & Reinisch, B. W. (2015). Ionospheric vertical plasma drift and electron density response during total solar eclipses at equatorial/low latitude. *Journal of Geophysical Research: Space Physics*, *120*, 8066–8084. https://doi.org/10.1002/2015JA021557

Adeniyi, J. O., Radicella, S. M., Adimula, I. A., Willoughby, A. A., Oladipo, O. A., & Olawepo, O. (2007). Signature of the 29 March 2006 eclipse on the ionosphere over an equatorial station. *Journal of Geophysical Research*, *112*, A06314. https://doi.org/10.1029/2006JA012197

Afraimovich, E. L., Kosogorov, E. A., & Lesyuta, O. S. (2002). Effects of the August 11, 1999 total solar eclipse as deduced from total electron content measurements at the GPS network. *Journal of Atmospheric and Solar-Terrestrial Physics*, *64*(18), 1933–1941, ISSN 1364–6826. https://doi.org/10.1016/S1364-6826(02)00221-3

Bailey, G. J., & Sellek, R. (1990). A mathematical model of the Earth's plasmasphere and its application in a study of He at $L = 3$. *Annales de Geophysique*, *8*(3), 171–189.

Bailey, G. J., Sellek, R., & Rippeth, Y. (1993). A modelling study of the equatorial topside ionosphere. *Annales de Geophysique*, *11*(4), 263–272.

Balan, N., Bailey, G. J., & Titheridge, J. E. (1995). Modelling studies of north-south differences in the ionosphere at mid latitudes. *Advances in Space Research*, *16*(5), 99–102. https://doi.org/10.1016/0273-1177(95)00177-g

Beynon, W. J. G. (1955). Solar eclipses and the ionosphere. *Nature*, *176*(4490), 947–948. https://doi.org/10.1038/176947a0

Bravo, M., Martínez-Ledesma, M., Foppiano, A., Urra, B., Ovalle, E., Villalobos, C., et al. (2020). First report of an eclipse from Chilean ionosonde observations: Comparison with total electron content estimations and the modeled maximum electron concentration and its height. *Journal of Geophysical Research: Space Physics*, *125*, e2020JA027923. https://doi.org/10.1029/2020JA027923

Bravo, M. A., Batista, I. S., Souza, J. R., & Foppiano, A. J. (2017). Equatorial ionospheric response to different estimated disturbed electric fields as investigated using Sheffield University Plasmasphere Ionosphere Model at INPE. *Journal of Geophysical Research: Space Physics*, *122*, 10,511–10,527. https://doi.org/10.1002/2017JA024265

Bravo, M. A., Batista, I. S., Souza, J. R., & Foppiano, A. J. (2019). Ionospheric response to disturbed winds during the 29 October 2003 geomagnetic storm in the Brazilian sector. *Journal of Geophysical Research: Space Physics*, *124*, 9405–9419. https://doi.org/10.1029/2019JA027187

Chen, C., Lin, C. C., & Matsuo, T. (2019). Ionospheric responses to the 21 August 2017 solar eclipse by using data assimilation approach. *Progress in Earth and Planetary Science*, *6*(1), 1–9. https://doi.org/10.1186/s40645-019-0263-4

Cheng, K. H., Huang, Y. N., & Chen, S. W. (1992). Ionospheric effects of the solar eclipse of September 23, 1987, around the equatorial anomaly crest region. *Journal of Geophysical Research*, *97*(A1), 103–111. https://doi.org/10.1029/91JA02409

Cnossen, I., Ridley, A. J., Goncharenko, L. P., & Harding, B. J. (2019). The response of the ionosphere-thermosphere system to the 21 August 2017 solar eclipse. *Journal of Geophysical Research: Space Physics*, *124*, 7341–7355. https://doi.org/10.1029/2018JA026402

Dang, T., Lei, J., Wang, W., Yan, M., Ren, D., & Huang, F. (2020). Prediction of the thermospheric and ionospheric responses to the 21 June 2020 annular solar eclipse. *Earth and Planetary Physics*, *4*, 231–237. https://doi.org/10.26464/epp2020032

Dang, T., Lei, J., Wang, W., Zhang, B., Burns, A., Le, H., et al. (2018). Global responses of the coupled thermosphere and ionosphere system to the August 2017 Great American Solar Eclipse. *Journal of Geophysical Research: Space Physics*, *123*, 7040–7050. https://doi.org/10.1029/2018JA025566

Evans, J. V. (1965a). On the behavior of f_oF_2 during solar eclipses. *Journal of Geophysical Research*, *70*, 733–738. https://doi.org/10.1029/JZ070i003p00733

Evans, J. V. (1965b). An F-region eclipse. *Journal of Geophysical Research*, *70*, 131–142. https://doi.org/10.1029/JZ070i001p00131

Fejer, B. G., Jensen, J. W., & Su, S.-Y. (2008). Quiet time equatorial *F* region vertical plasma drift model derived from ROCSAT-1 observations. *Journal of Geophysical Research*, *113*, A05304. https://doi.org/10.1029/2007JA012801

Frissell, N. (2017). w2naf/eclipse_calculator v1.0 (Version v1.0). Zenodo. https://doi.org/10.5281/zenodo.1120440

Goncharenko, L. P., Erickson, P. J., Zhang, S. R., Galkin, I., Coster, A. J., & Jonah, O. F. (2018). Ionospheric response to the solar eclipse of 21 August 2017 in Millstone Hill (42N) observations. *Geophysical Research Letters*, *45*, 4601–4609. https://doi.org/10.1029/2018GL077334

Hairston, M. R., Mrak, S., Coley, W. R., Burrell, A., Holt, B., Perdue, M., et al. (2018). Topside ionospheric electron temperature observations of the 21 August 2017 eclipse by DMSP spacecraft. *Geophysical Research Letters*, *45*, 7242–7247. https://doi.org/10.1029/2018GL077381

He, L., Heki, K., & Wu, L. (2018). Three-dimensional and trans-hemispheric changes in ionospheric electron density caused by the great solar eclipse in North America on 21 August 2017. *Geophysical Research Letters*, *45*, 10,933–10,940. https://doi.org/10.1029/2018GL080365

Hedin, A. E., Fleming, E. L., Manson, A. H., Schmidlin, F. J., Avery, S. K., Clark, R. R., et al. (1996). Empirical wind model for the upper, middle and lower atmosphere. *Journal of Atmospheric and Terrestrial Physics*, *58*(13), 1421–1447. https://doi.org/10.1016/0021-9169(95)00122-0

Huba, J. D., & Drob, D. (2017). SAMI3 prediction of the impact of the 21 August 2017 total solar eclipse on the ionosphere/plasmasphere system. *Geophysical Research Letters*, *44*, 5928–5935. https://doi.org/10.1002/2017GL073549

Huba, J. D., Joyce, G., & Fedder, J. A. (2000). Sami2 is Another Model of the Ionosphere (SAMI2): A new low-latitude ionosphere model. *Journal of Geophysical Research*, *105*(A10), 23,035–23,053. https://doi.org/10.1029/2000JA000035

Jonah, O. F., Goncharenko, L., Erickson, P. J., Zhang, S., Coster, A., Chau, J. L., et al. (2020). Anomalous behavior of the equatorial ionization anomaly during the 2 July 2019 solar eclipse. *Journal of Geophysical Research: Space Physics*, *125*, e2020JA027909. https://doi.org/10.1029/2020JA027909

Jose, L., Vineeth, C., Pant, T. K., & Kumar, K. K. (2020). Response of the equatorial ionosphere to the annular solar eclipse of 15 January 2010. *Journal of Geophysical Research: Space Physics*, *125*, e2019JA027348. https://doi.org/10.1029/2019JA027348

Le, H., Liu, L., Ding, F., Ren, Z., Chen, Y., Wan, W., et al. (2010). Observations and modeling of the ionospheric behaviors over the East Asia zone during the 22 July 2009 solar eclipse. *Journal of Geophysical Research*, *115*, A10313. https://doi.org/10.1029/2010JA015609

Le, H., Liu, L., Yue, X., & Wan, W. (2008a). The midlatitude F_2 layer during solar eclipses: Observations and modeling. *Journal of Geophysical Research*, *113*, A08309. https://doi.org/10.1029/2007JA013012

Le, H., Liu, L., Yue, X., & Wan, W. (2008b). The ionospheric responses to the 11 August 1999 solar eclipse: Observations and modeling. *Annales Geophysicae*, *26*, 107–116. https://doi.org/10.5194/angeo-26-107-2008

Le, H., Liu, L., Yue, X., & Wan, W. (2009). The ionospheric behavior in conjugate hemispheres during the 3 October 2005 solar eclipse. *Annales Geophysicae*, *27*(1), 179–184. https://doi.org/10.5194/angeo-27-179-2009

Le, H., Liu, L., Yue, X., Wan, W., & Ning, B. (2009). Latitudinal dependence of the ionospheric response to solar eclipses. *Journal of Geophysical Research*, *114*, A07308. https://doi.org/10.1029/2009JA014072

Lee, C. C., Reinisch, B. W., Su, S.-Y., & Chen, W. S. (2008). Quiet-time variations of F_2-layer parameters at Jicamarca and comparison with IRI-2001 during solar minimum. *Journal of Atmospheric and Solar-Terrestrial Physics*, *70*, 1184–1192, ISSN 1364-6826. https://doi.org/10.1016/j.jastp.2007.10.008

Lei, J., Dang, T., Wang, W., Burns, A., Zhang, B., & Le, H. (2018). Long-lasting response of the global thermosphere and ionosphere to the 21 August 2017 solar eclipse. *Journal of Geophysical Research: Space Physics*, *123*, 4309–4316. https://doi.org/10.1029/2018JA025460

Li, Q., Hao, Y., Zhang, D., & Xiao, Z. (2018). Nighttime enhancements in the midlatitude ionosphere and their relation to the plasmasphere. *Journal of Geophysical Research: Space Physics*, *123*, 7686–7696. https://doi.org/10.1029/2018JA025422

Li, Z., Luan, X., & Ren, D. (2019). Longitudinal variations of the occurrence probability of the ionospheric F_1 layer peak at middle and high latitudes. *Journal of Geophysical Research: Space Physics*, *124*, 9592–9609. https://doi.org/10.1029/2018JA026236

MacPherson, B., González, S. A., Sulzer, M. P., Bailey, G. J., Djuth, F., & Rodriguez, P. (2000). Measurements of the topside ionosphere over Arecibo during the total solar eclipse of February 26, 1998. *Journal of Geophysical Research*, *105*(A10), 23,055–23,067. https://doi.org/10.1029/2000JA000145

Madhav Haridas, M. K., & Manju, G. (2012). On the response of the ionospheric F region over Indian low-latitude station Gadanki to the annular solar eclipse of 15 January 2010. *Journal of Geophysical Research*, *117*, A01302. https://doi.org/10.1029/2011JA016695

McInerney, J. M., Marsh, D. R., Liu, H.-L., Solomon, S. C., Conley, A. J., & Drob, D. P. (2018). Simulation of the 21 August 2017 solar eclipse using the Whole Atmosphere Community Climate Model-eXtended. *Geophysical Research Letters*, *45*, 3793–3800. https://doi.org/10.1029/2018GL077723

Mrak, S., Semeter, J. L., Drob, D., & Huba, J. D. (2018). Direct EUV/X-ray modulation of the ionosphere during the August 2017 total solar eclipse. *Geophysical Research Letters*, *45*, 3820–3828. https://doi.org/10.1029/2017GL076771

Müller-Wodarg, I. C. F., Aylward, A. D., & Lockwood, M. (1998). Effects of a mid-latitude solar eclipse on the thermosphere and ionosphere—A modelling study. *Geophysical Research Letters*, *25*(20), 3787–3790. https://doi.org/10.1029/1998GL900045

Niehuss, K. O., Euler, H. C., & Vaughan, W. W. (1996). *Statistical technique for intermediate and long-range estimation of 13-month smoothed solar flux and geomagnetic index. NASA Technical Memorandum 4759, September 1996, Marshall Space Flight Center*. Alabama: National Aeronautics and Space Administration at George C. Marshall Space Flight Center. Retrieved from https://ntrs.nasa.gov/archive/nasa/casi.ntrs.nasa.gov/19960048010.pdf

Nogueira, P. A. B., Abdu, M. A., Souza, J. R., Bailey, G. J., Batista, I. S., Shume, E. B., & Denardini, C. M. (2013). Longitudinal variation in Global Navigation Satellite Systems TEC and topside ion density over South American sector associated with the four-peaked wave structures. *Journal of Geophysical Research: Space Physics*, *118*, 7940–7953. https://doi.org/10.1002/2013JA019266

Perry, G. W., Watson, C., Howarth, A. D., Themens, D. R., Foss, V., Langley, R. B., & Yau, A. W. (2019). Topside ionospheric disturbances detected using radio occultation measurements during the August 2017 solar eclipse. *Geophysical Research Letters*, *46*, 7069–7078. https://doi.org/10.1029/2019GL083195

Peterson, W. K., Stavros, E. N., Richards, P. G., Chamberlin, P. C., Woods, T. N., Bailey, S. M., & Solomon, S. C. (2009). Photoelectrons as a tool to evaluate spectral variations in solar EUV irradiance over solar cycle timescales. *Journal of Geophysical Research*, *114*, A10304. https://doi.org/10.1029/2009JA014362

Pezzopane, M., Zuccheretti, E., Bianchi, C., Scotto, C., Zolesi, B., Cabrera, M. A., & Ezquer, R. G. (2007). The new ionospheric station of Tucumán: First results. *Annals of Geophysics*, *50*(3), 483–492. ISSN 2037-416X. https://doi.org/10.4401/ag-4426

Picone, J. M., Hedin, A. E., Drob, D. P., & Aikin, A. C. (2002). NRLMSISE-00 empirical model of the atmosphere: Statistical comparisons and scientific issues. *Journal of Geophysical Research*, *107*(A12), 1468. https://doi.org/10.1029/2002JA009430

Ratcliffe, J. A. (1956). A survey of solar eclipses and the ionosphere. In W. J. G. Beynon & G. M. Brown (Eds.), *Solar eclipses and the ionosphere* (pp. 1–13). Oxford: Pergamon Press.

Reinisch, B., & Huang, X. (1996). The F1 ledge: Density, height and slope. *Annals of Geophysics*, *39*(4). https://doi.org/10.4401/ag-4022

Reinisch, B. W., Dandenault, P. B., Galkin, I. A., Hamel, R., & Richards, P. G. (2018). Investigation of the electron density variation during the 21 August 2017 solar eclipse. *Geophysical Research Letters*, *45*, 1253–1261. https://doi.org/10.1002/2017GL076572

Richards, P. G., Meier, R. R., & Wilkinson, P. J. (2010). On the consistency of satellite measurements of thermospheric composition and solar EUV irradiance with Australian ionosonde electron density data. *Journal of Geophysical Research*, *115*, A10309. https://doi.org/10.1029/2010JA015368

Richards, P. G., Woods, T. N., & Peterson, W. K. (2006). HEUVAC: A new high resolution solar EUV proxy model. *Advances in Space Research*, *37*(2), 315–322. https://doi.org/10.1016/j.asr.2005.06.031

Rishbeth, H. (1968). Solar eclipses and ionospheric theory. *Space Science Reviews*, *8*(4), 543–554. https://doi.org/10.1007/BF00175006

Roble, R. G., Emery, B. A., & Ridley, E. C. (1986). Ionospheric and thermospheric response over Millstone Hill to the May 30, 1984, annular solar eclipse. *Journal of Geophysical Research*, *91*(A2), 1661–1670. https://doi.org/10.1029/JA091iA02p01661

Salah, J. E., Oliver, W. L., Foster, J. J., Holt, J. M., Emery, B. A., & Roble, R. G. (1986). Observation of the May 30, 1984, annular solar eclipse at Millstone Hill. *Journal of Geophysical Research*, *91*(A2), 1651–1660.

Santos, A. M., Abdu, M. A., Souza, J. R., Sobral, J. H. A., & Batista, I. S. (2016). Disturbance zonal and vertical plasma drifts in the Peruvian sector during solar minimum phases. *Journal of Geophysical Research: Space Physics*, *121*, 2503–2521. https://doi.org/10.1002/2015JA022146

Schunk, R. W., & Nagy, A. F. (2009). *Ionospheres* (Second ed.). New York: Cambridge Univ. Press.

Sergeenko, N. P. (2018). Irregular phenomena in magnetically conjugate regions of the F_2 layer of the ionosphere. *Geomagnetism and Aeronomy*, *58*(6), 823–830. https://doi.org/10.1134/S0016793218060166

Souza, J., Brum, C., Abdu, M., Batista, I., Asevedo, W., Bailey, G., & Bittencourt, J. (2010). Parameterized regional ionospheric model and a comparison of its results with experimental data and IRI representations. *Advances in Space Research*, *46*, 1032–1038. https://doi.org/10.1016/j.asr.2009.11.025

Souza, J. R., Asevedo, W. D. Jr., dos Santos, P. C. P., Petry, A., Bailey, G. J., Batista, I. S., & Abdu, M. A. (2013). Longitudinal variation of the equatorial ionosphere: Modeling and experimental results. *Advances in Space Research*, *51*, 654–660. https://doi.org/10.1016/j.asr.2012.01.023

Sridharan, R., Devasia, C. V., Jyoti, N., Tiwari, D., Viswanathan, K. S., & Subbarao, K. S. V. (2002). Effects of solar eclipse on the electrodynamical processes of the equatorial ionosphere: A case study during 11 August 1999 dusk time total solar eclipse over India. *Annales de Geophysique*, *20*(12), 1977–1985. https://doi.org/10.5194/angeo-20-1977-2002

Sterling, D. L., Hanson, W. B., & Woodman, R. F. (1972). Synthesis of data obtained at Jicamarca, Peru, during the September 11, 1969, eclipse. *Radio Science*, *7*(2), 279–289. https://doi.org/10.1029/RS007i002p00279

Strickland, D. J., Lean, J. L., Daniell, R. E. Jr., Knight, H. K., Woo, W. K., Meier, R. R., et al. (2007). Constraining and validating the Oct/Nov 2003 X-class EUV flare enhancements with observations of FUV dayglow and E-region electron densities. *Journal of Geophysical Research*, *112*, A06313. https://doi.org/10.1029/2006JA012074

Strobel, D. F., Young, T. R., Meier, R. R., Coffey, T. P., & Ali, A. W. (1974). The nighttime ionosphere: *E* region and lower *F* region. *Journal of Geophysical Research*, *79*(22), 3171–3178. https://doi.org/10.1029/JA079i022p03171

Thampi, S. V., Balan, N., Lin, C., Liu, H., & Yamamoto, M. (2011). Mid-latitude Summer Nighttime Anomaly (MSNA)—Observations and model simulations. *Annales de Geophysique*, *29*, 157–165. https://doi.org/10.5194/angeo-29-157-2011

Tomás, A. T., Lühr, H., Förster, M., Rentz, S., & Rother, M. (2007). Observations of the low-latitude solar eclipse on 8 April 2005 by CHAMP. *Journal of Geophysical Research*, *112*, A06303. https://doi.org/10.1029/2006JA012168

Tsai, H. F., & Liu, J. Y. (1999). Ionospheric total electron content response to solar eclipses. *Journal of Geophysical Research*, *104*(A6), 12,657–12,668. https://doi.org/10.1029/1999JA900001

Unnikrishnan, K., & Richards, P. (2014). How does solar eclipse influence the complex behavior of midlatitude ionosphere? Two case studies. *Journal of Geophysical Research: Space Physics*, *119*, 1157–1171. https://doi.org/10.1002/2013JA018708

Verhulst, T. G. W., & Stankov, S. M. (2020). Height dependency of solar eclipse effects: The ionospheric perspective. *Journal of Geophysical Research: Space Physics*, *125*, e2020JA028088. https://doi.org/10.1029/2020JA028088

Wang, W., Dang, T., Lei, J., Zhang, S., Zhang, B., & Burns, A. (2019). Physical processes driving the response of the F_2 region ionosphere to the 21 August 2017 solar eclipse at Millstone Hill. *Journal of Geophysical Research: Space Physics*, *124*, 2978–2991. https://doi.org/10.1029/2018JA025479

Woods, T. N., Chamberlin, P. C., Peterson, W. K., Meier, R. R., Richards, P. G., Strickland, D. J., et al. (2008). XUV photometer system (XPS): Improved solar irradiance algorithm using CHIANTI spectral models. *Solar Physics*, *250*(2), 235–267. https://doi.org/10.1007/s11207-008-9196-6

Woods, T. N., Eparvier, F. G., Bailey, S. M., Chamberlin, P. C., Lean, J., Rottman, G. J., et al. (2005). Solar EUV Experiment (SEE): Mission overview and first results. *Journal of Geophysical Research*, *110*, A01312. https://doi.org/10.1029/2004JA010765

Wu, C., Ridley, A. J., Goncharenko, L., & Chen, G. (2018). GITM-data comparisons of the depletion and enhancement during the 2017 solar eclipse. *Geophysical Research Letters*, *45*, 3319–3327. https://doi.org/10.1002/2018GL077409

Yau, A. W., Foss, V., Howarth, A. D., Perry, G. W., Watson, C., & Huba, J. (2018). Eclipse-induced changes to topside ion composition and field-aligned ion flows in the August 2017 solar eclipse: e-POP observations. *Geophysical Research Letters*, *45*, 10,829–10,837. https://doi.org/10.1029/2018GL079269